New performance maps for selecting suitable small-scale turbine configuration for low-power organic Rankine cycle applications

Al Jubori, Ayad M.; Al-dadah, Raya; Mahmoud, Saad

DOI:
10.1016/j.jclepro.2017.05.177

Document Version
Peer reviewed version

Citation for published version (Harvard):
Al Jubori, AM, Al-dadah, R & Mahmoud, S 2017, 'New performance maps for selecting suitable small-scale turbine configuration for low-power organic Rankine cycle applications', *Journal of Cleaner Production*. https://doi.org/10.1016/j.jclepro.2017.05.177

Accepted Manuscript

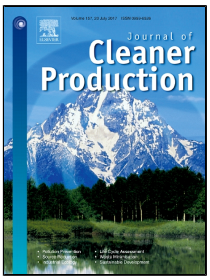

New performance maps for selecting suitable small-scale turbine configuration for low-power organic Rankine cycle applications

Ayad M. Al Jubori, Raya Al-Dadah, Saad Mahmoud

PII:	S0959-6526(17)31129-0
DOI:	10.1016/j.jclepro.2017.05.177
Reference:	JCLP 9717
To appear in:	*Journal of Cleaner Production*
Received Date:	02 March 2017
Revised Date:	25 May 2017
Accepted Date:	28 May 2017

Please cite this article as: Ayad M. Al Jubori, Raya Al-Dadah, Saad Mahmoud, New performance maps for selecting suitable small-scale turbine configuration for low-power organic Rankine cycle applications, *Journal of Cleaner Production* (2017), doi: 10.1016/j.jclepro.2017.05.177

New performance maps for selecting suitable small-scale turbine configuration for low-power organic Rankine cycle applications

Ayad M. Al Jubori [a,b *], Raya Al-Dadah [a], Saad Mahmoud [a]

[a] The University of Birmingham, School of Engineering, Edgbaston, Birmingham, B15 2TT, UK
[b] University of Technology, Baghdad, Iraq
[*]Email: ama232@bham.ac.uk, ayadms@gmail.com

Abstract

This paper aims to deliver new performance maps for small-scale organic Rankine cycle (ORC) turbines (<20 kW) by assessing the impact of single and two stage turbine configurations on the ORC's performance driven by low-temperature (<100 °C) heat source. Small-scale axial, radial-inflow and radial-outflow turbines are designed and compared with their single and two stage configurations in order to enhance the performance of the ORC's system by increasing its expansion ratio. Therefore, the preliminary mean-line design is coupled with three-dimensional CFD analysis and ORC modelling for all turbines' configurations to deliver the performance maps for low-power applications. Due to the complex and 3D nature of flow across the turbine, CFD analysis was used to investigate in more detail five candidates of small-scale turbines, in single and two stage configurations with three working fluids (R141b, R245fa and isopentane). ANSYS®17-CFX was used to perform 3D CFD analysis of all turbine configurations. RANS equations for three-dimensional steady state and viscous flow were solved with a k-ω SST turbulence model. The performance maps in terms of turbine efficiency and power for each turbine configuration are presented according to the operating conditions in terms of expansion ratio, working fluid mass flow rate, and rotational speed with turbine size.

The results revealed that the two-stage axial and radial-outflow turbines' configurations exhibited a considerably higher turbine performance, with overall isentropic efficiency of 84.642% and 82.9% and power output of 15.798 kW and 14.331 kW respectively, with R245fa as a working fluid. Also, the results exhibited that the maximum ORC thermal efficiency for both two-stage configurations was 13.96% and 12.80% for axial and radial-outflow turbines respectively working with R245fa. These results indicated the potential advantages of a two-stage turbine configuration in a small-scale ORC system for the conversion of a low-temperature heat source into electricity as a useful power.

Keywords: organic Rankine cycle (ORC); small-scale; single and two-stage turbines' configurations; CFD; organic working fluids.

Nomenclature

A	area (m^2)
B	constant of tip clearance loss (-)
b	axial chord (m)/tip width (m)
C	absolute velocity (m s^{-1})
c	chord length (m)
C_L	lift coefficient (-)
D, d	diameter (m)
d_s	specific diameter (-)
f	correction/friction coefficient's (-)
h	specific enthalpy (kJ/kg)
H	blade height (m)
l	length (m)
K	losses coefficient (-)
k	specific turbulence kinetic energy (m^2 s^{-2})
$\dot{m}$	mass flow rate (kg s^{-1})
N	number of blade (-)
n_s	specific speed (-)
o	throat (m)
P	pressure (bar)
$\dot{Q}$	heat (kW)
R_n	reaction (-)
r	radius (m)
S	blade space (pitch) (m)
s	entropy (kJ $kg^{-1}.K^{-1}$)
T	temperature (K)
t	time (s)/ blade thickness (m)
U	blade velocity (m/s)/ mean flow velocity (m s^{-1})
V	velocity (m/s)
W	relative velocity (m s^{-1})
w	specific work (kJ kg^{-1})
$\dot{W}$	power (kW)

Greek symbols

α	absolute flow angle (degree)
β	relative flow angle (degree)
η	efficiency (%)
ε	clearance (m)
ϕ	flow coefficient (-)
ψ	loading coefficient (-)
ω	specific turbulence dissipation rate (m^2 sec^{-3})
Ω	angular velocity (rad s^{-1})
ρ	density (kg m^{-3})
τ	tip clearance (m)
ζ	enthalpy loss coefficient (-)

Subscript/superscript

1-7	station within the turbine and cycle respectively.
accel	accelerating
AS	aspect ratio
blds	blade
cr	critical
e	evaporator
ex	exergy
f	friction
H	high
hyd	hydraulic
is	isentropic
L	low
m	mean
nbp	normal boiling point
P	profile
p	pump
R	rotor
Re	Reynolds number
S	stator
Sec	secondary
sec eff	second law efficiency
sh	shock
T	total
t	turbine/tip
th	thermal
TC	tip clearance
TE	trailing edge
ts	total-to-static
tt	total-to-total
x	axial
θ	tangential/circumferential direction
*	uncorrected

Acronyms

1D, 3D	one and three dimensional
AFT	axial flow turbine
BDA	blade geometric discharge angle
CFD	computational fluid dynamics
EES	Engineering Equation Solver
GWP	global warming potential
ODP	ozone depletion potential
ORC	organic Rankine cycle
PD	preliminary mean-line design
RANS	Reynolds-averaged Navier-Stokes
RIT	radial-inflow turbine
ROT	radial-outflow turbine
SST	shear stress transport

1. Introduction

Recently, with increasing concern regarding the climate change and the need for sustainable efficient power system has led to a huge attention in organic Rankine cycle (ORC) technologies. Particularly with low power output and low-temperature heat sources (<100 °C), for a small-scale system, further development is still vital to achieve efficient small-scale ORC turbines. Some ORC systems based on small-scale single and two-

stage turbines are applicable for various low-power generation applications (<20 kW), such as in domestic and rural areas and remote off-grid communities.

The preliminary mean-line design (PD) model of small-scale turbines (i.e. axial and radial turbines) based on losses model has been considered in many studies in literature. However, the limitation with preliminary mean-line design model of turbine, it is developed for obtaining velocity triangles, turbine dimensions without consideration for flow inside the stator/rotor passage, which has effectively influence on providing efficient expansion through the passage.

In terms of 3D CFD analysis for the radial-inflow turbine (RIT), Harinck et al. (2013) achieved it for a Tri-O-Gen RIT with 2D optimization for the stator. It was manufactured and tested for a 5 kW ORC system with toluene as the working fluid. Sauret and Gu (2014) completed a 3D simulation process of a 400 kW ORC RIT with R143a as the working fluid at mass flow rate of 17.24 kg/s for geothermal applications. Their results showed the maximum isentropic efficiency of 83.5%. Fiaschi et al. (2016) performed mean-line design and 3D CFD simulation of the rotor of a micro ORC RIT based on R134a as the working fluid at a mass flow rate of 0.25 kg/s. Their results indicated that the maximum variation between the PD and CFD was 11.6% in terms of power output. The CFD results showed that the turbine isentropic efficiency of 71.76% and power of 5.162 kW were achieved. Russell et al. (2016) completed a design and simulation process for a 7 kW ORC RIT. The maximum turbine efficiency was about 76%, with R245fa as the working fluid. Li and Ren (2016) carried out 3D CFD simulation for the RIT with R123 as the working fluid at mass flow rate of 21.2 kg/s and expansion ratio of 8. The turbine isentropic efficiency, system thermal efficiency and net power were 84.33%, 13.5% and 534 kW respectively. Rahbar et al. (2016) optimized the transonic rotor of a two-stage RIT working with R245fa and an expansion ratio of 10, using the genetic algorithm. The optimization results indicated that the maximum turbine and ORC system's efficiencies were 88% and 14.8% respectively, corresponding to the power output of 26.35 kW at the mass flow rate of 0.8768 kg/s.

For an axial flow turbine (AFT), Moroz et al. (2013) presented the detailed design of a 250 kW AFT for an ORC power unit with R245fa at low-temperatures up to 150 °C. The structural optimization was carried out to reduce the rotor weight to an acceptable stress. The reported turbine efficiency achieved as a result from the turbine optimization was 81.7%. Al Jubori et al. (2016) developed a micro-scale ORC based on single-stage axial and radial-inflow turbines and five organic fluids for low-temperature heat sources. The PD and three-dimensional CFD analysis were conducted for both configurations. The results showed that the AFT was competitive to the RIT at the mass flow rate of 0.5 kg/s with the maximum ORC efficiency of 10.60% based on

the RIT compared with 10.14% based on the AFT. Al Jubori et al. (2017a) also developed a new methodology that integrated small-scale ORC system modelling with 1D, 3D CFD analysis and optimization of the single-stage AFT based on a multi-objective genetic algorithm (MOGA). As the working fluids, six organic fluids were investigated. The optimization results exhibited that the maximum turbine and ORC efficiencies and power output were 88%, 10.5% and 6.3 kW respectively with R123 working fluid.

While for a radial-outflow turbine (ROT), Persico et al. (2015) performed three-dimensional CFD aerodynamic analysis of small-scale ROT cascades. The results showed the efficiency obtained by CFD analysis to be higher than estimated by a preliminary design model. Al Jubori et al. (2017b) performed 1D and 3D CFD analysis of small-scale ORC based on single-stage axial and radial outflow turbines with five working fluid namely (R141b, R245fa, R365mfc, isobutane, n-pentane). Their results showed that the maximum turbine performance was based on axial configuration with turbine efficiency of 82.5% and a power output of 15.15 kW at mass flow rate of 0.7 kg/s.

In terms of experimental investigation, Pei et al. (2011) designed and tested an RIT for an ORC system with R123 as the working fluid and the inlet turbine temperature of about 100 °C. Their experimental results showed the turbine and ORC thermal efficiencies of 65% and 6.8% respectively. Kang (2012) constructed an ORC system based on an RIT operating with R245fa. The experimental results exhibited that the turbine and ORC's efficiencies were 78.7% and 5.22% with power of 32.7 kW. Ssebabi et al. (2015) manufactured the rotor for the RIT kit for low-grade waste heat recovery application with R123 as the working fluid. Their experimental performance had very low isentropic efficiency between (6-10%). Pu et al. (2016) performed an experimental study of a small-scale axial turbine for ORC system based on HFE7100 and R245fa as the working fluids. Their results exhibited the turbine and cycle efficiencies were 59.7% and 4.01% respectively with corresponding power of 1.979 kW. Kang (2016) investigated experimentally a two-stage RIT to improve the ORC's system performance with an expansion ratio of 11.6 and an evaporator temperature of 116 °C. The results indicated the turbine and ORC system's efficiencies and power were 68.5%, 9.8% and 39.0 kW respectively.

The accurate evaluation of the achievable small-scale ORC turbine performance (i.e. efficiency and power) entails experimental data which is currently lacking and costly in terms of a prototype. Therefore, there is need for a more advanced technique such as using 3D CFD analysis, to deliver more accurate prediction regarding small-scale ORC turbines' performance. Consequently, this paper aims to present new performance maps for the small-scale ORC system powered by low-grade heat sources (<100 °C) and the low-mass flow rate based on

various candidate turbines namely: axial, radial-inflow and radial-outflow turbines, in single and two stage configurations. The developed mean-line design, 3D CFD analysis and ORC system modelling were integrated to achieve an accurate prediction for different working fluids and operating conditions, for small-scale ORC turbines and low-power applications (i.e. <20 kW). The difference between the current research and the previous research (Al Jubori et al., 2016) and other literature mentioned-above, the new performance maps are presented in the current work for five turbine configurations including: single stage radial-inflow, axial flow and radial outflow, and two stage axial flow and radial-outflow turbines. The performance maps in terms of the non-dimensional parameters namely: specific speed and specific diameter, are introduced that can be readily used by the researchers with different operating conditions such as rotational speed and expansion ratio. The ranges for each turbine configuration in terms of turbines performance (efficiency and power) are offered. Furthermore, the cycle thermal efficiency has been presented in terms of mass flow rate and turbine total inlet temperature for five turbine configurations. Furthermore, there exists a gap in the knowledge concerning the development of the performance maps for the efficient configuration of small-scale turbines for low power output capacity. This paper offers a better understanding of the performance maps for five small-scale turbines' configurations by providing more results of turbine performance (efficiency and power output), cycle thermal efficiency and turbines size with various organic fluids. Therefore, the mean-line design models of the turbines and ORC's system modelling were implemented using the Engineering Equation Solver (EES); while ANSYS^{R17}-CFX was used to investigate the turbine performance and three-dimensional viscous flow based on real gas formulation.

2.1 Selection of organic working fluids

The selection of the organic working fluids in ORC system modelling is considered as one of the most critical parameters because of the enormous ranges of the prospective applications for the available heat sources' temperatures, the expander's type, power size and environmental levels. This is highlighted by the abundance of literature (e.g. Tchanche et al., 2011; Bao and Zhao, 2012), where it is recognised that there is no single organic fluid that will fulfil all the preferred standards and the designers need to choice the optimal working fluid based on their applications. Also, the thermo-physical properties of the organic fluids have a significant influence on turbine ORC's system efficiencies, size and performance, safety and stability (i.e. critical pressure and temperature) and environmental impact. Also, there are additional practical criteria which should be considered in the selection of organic fluids such as the global warming potential (GWP), the ozone depletion potential (ODP), safety and life time, as tabulated in Table 1. Based on the slope of the saturation

vapour of the organic fluid on the T-s diagram, it is characterised into dry, isentropic and wet organic fluids. The dry and isentropic organic fluids are more suitable for low-grade temperature applications since the expansion after the turbine will be in the superheated zone as presented on the T-s (i.e. Temperature-entropy) diagram in Fig. 1a and b. This feature considerably reduces the turbine maintenance and evaporator size requirements, leading to a reduced capital cost of the ORC system by alleviating concerns about the existence of liquid droplets of working fluid in the rotor stage, i.e. without needing to the preheat equipment, as shown in Fig. 1a and b. In Table 1, the working fluids are selected based on these criteria, and they are recommended in literature as a suitable for low temperature heat sources application. Moreover, according to their slopes of the saturation vapor curve are classified as dry working fluids (Bao and Zhao, 2012).

Table 1 Summary of physical and environmental properties for three working fluids.

Fluid	Mol. weight (g/mol)	T_{nbp} (K)	T_{cr} (K)	P_{cr} (kPa)	ODP	GWP (100 yr)
R141b	116.95	305.05	480	4460	0.12	725
R245fa	134.05	288.14	426	3610	0	950
Isopentane	72.149	300.98	460.35	3378	0	20

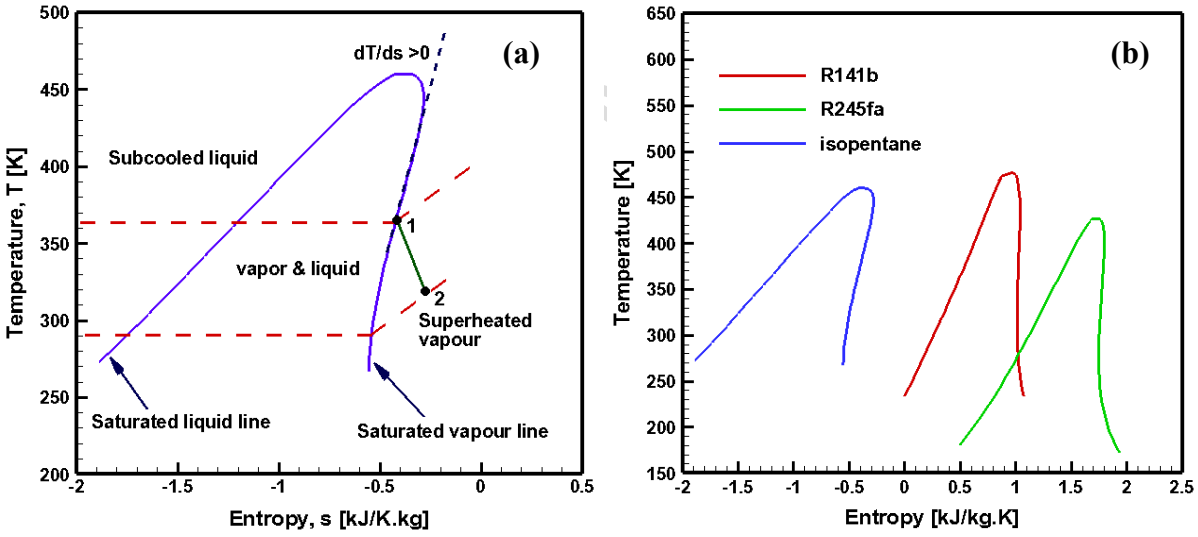

Fig.1. T-s diagram of dry organic fluid (a), T-s diagram of three investigated fluids (b).

2.2 Organic Rankine cycle (ORC) system modelling

The recuperative organic Rankine cycle includes evaporator, turbine, condenser, recuperator and pump as shown in Fig. 2. In the present work, the subcritical ORC system is investigated to avoid the complexity and alleviation concerns regarding to safety and high-pressure systems. The assumptions of steady-state operating condition and neglecting the pressure and heat losses through the connected pipes in the ORC system are considered. The heat added from the heat source is obtained from equation (1) as following:

$$\dot{Q}_e = \dot{m}(h_1 - h_7) \quad (1)$$

The power output from the turbine is given by:

$$\dot{W}_t = \dot{m}(h_1 - h_{2is})\eta_{t1} + \dot{m}(h_2 - h_{3is})\eta_{t2} \quad (2)$$

The delivered net power output from the system is determined using following equation:

$$\dot{W}_{net} = \dot{W}_t \eta_{mech} \eta_{gen} - \dot{W}_p \quad (3)$$

where the η_{gen} and η_{mech} are the generator and mechanical efficiencies respectively.

The thermal efficiency of ORC system is determined by:

$$\eta_{th} = \frac{\dot{W}_{net}}{\dot{Q}_e} \quad (4)$$

The ORC system second law efficiency is the ratio of the actual ORC thermal efficiency to the ideal system efficiency i.e. Carnot cycle efficiency which is obtained using the following equation:

$$\eta_{sec\ eff} = \frac{\eta_{th}}{\eta_{Carnot}} = \frac{\dot{W}_{net}}{\dot{Q}_e\left(1 - \frac{T_L}{T_H}\right)} \quad (5)$$

The details of input parameters in terms of heat and sink sources' temperatures (i.e. hot side temperature and cold side temperature) for the ORC's system modelling and turbines design is outlined in Table 2 with different ranges of mass flow rate (0.1-0.5 kg/s). The design input parameters of the ORC's system modelling and turbine design are detailed in Table 2. The design parameter values are stated in terms of heat source temperature and heat sink temperature (cold side temperature) with three organic working fluids for various ranges of mass flow rates within 0.1-0.5 kg/s. Where the working fluid mass flow rate is used as an input parameter to calculate the desired power output, thus the ORC system and the turbine design can be sized to achieve this specification.

Table 2 Input parameters used in the ORC modelling.

Parameters	Values/Ranges	Unit
Temperature of heat source	365	K
Temperature of heat sink	293	K
Recuperator effectiveness	80%	-
Pump efficiency	75%	-
Mechanical efficiency	96%	-
Generator efficiency	96%	-
Mass flow rate of working fluids	0.1-0.5	kg/s
Working fluids	R141b, R245fa and isopentane	-

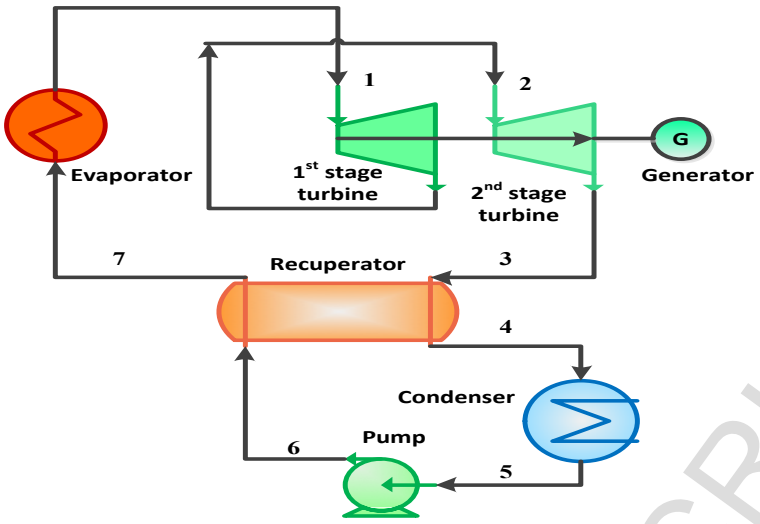

Fig. 2. The recuperative ORC schematic diagram.

3. Turbine preliminary mean-line design (PD)

The initial and crucial step in the whole of turbine design is the preliminary mean-line design (PD); it is a one-dimensional flow analysis and approximation at the mean radius of the turbine stage. Therefore, it can be classified as a low-fidelity model; it needs the implementation of correlations to predict losses, turbine performance and blade geometry. In the PD, the flow at the mid-span of the blade passage is assumed uniform and unidirectional by only focusing on the conditions at the inlet and outlet of each blade passage, regardless of the specifics of the blade geometry. Based on these simplifications, the PD model allows a quick evaluation of the turbine's performance, thermodynamic process and flow at the inlet and exit of the blade passage throughout the velocity triangles. Thus, PD analysis can deliver initial realistic assessments of turbine performance and layout in terms velocity triangles, blade geometry and height, number of blades and turbine size. Turbine efficiency and pressure ratio are significantly affecting the ORC system's performance. A single-stage turbine has a typical maximum pressure ratio of around 4 (Balje, 1981); thus, under high-pressure ratio operation, the design of a two-stage turbine can compensate for this limitation/drawback.

3.1 Axial-flow turbine (AFT) design

The turbine's dimensions and blade geometry (blade chord, throat width, blade pitch and number of blades, blade thickness at leading and trailing edges) are delivered from the PD of the axial-flow turbine (AFT) as detailed by Wilson and Korakianitis (2014). Three dimensionless parameters namely the degree of reaction (R_n), flow (ϕ) and loading (ψ) coefficients are applied to estimate the initial turbine efficiency and obtain the velocity triangles of the blade's passage, as presented in equations (6) and (7) (Japikse and Baines, 1994; Moustapha et al., 2003). As can be seen in Fig. 3, the fluid enters the stator by the flow angle (α_1) and absolute velocity (C_1)

then exit by the flow angle (α_2) and absolute velocity (C_2). Then the flow comes in the rotor with relative angle (β_2) and velocity (W_2) where the flow of the working fluid is speeded up to the relative velocity (W_3) with the relative angle (β_3) at the exit of the turbine's rotor. In a single-stage axial turbine, $\alpha_1=0$; while, $\alpha_1=\alpha_3$ in a multi-stage axial turbine. The flow angles at the inlet and outlet of the blade's passage (stator and rotor) are given by the following equations (Japikse and Baines, 1994; Moustapha et al., 2003):

$$\left.\begin{aligned} \tan\beta_2 &= \frac{(\Psi - 2R_n)}{2\phi} \\ \tan\beta_3 &= \frac{-(\Psi + 2R_n)}{2\phi} \\ \tan\alpha_3 &= \frac{-\left(\Psi/2 - (1 - R_n)\right)}{\phi} \\ \tan\alpha_2 &= \frac{\left(\Psi/2 + (1 - R_n)\right)}{\phi} \end{aligned}\right\} \quad (6)$$

The expressions of the degree of reaction, flow and loading coefficient are as follows:

$$\left.\begin{aligned} R_n &= \frac{\Delta h_{rotor}}{\Delta h_{stage}} \\ \emptyset &= \frac{C_x}{U} \\ \Psi &= \frac{w}{U^2} = \frac{\Delta h_{stage}}{(r_m\Omega)^2} \end{aligned}\right\} \quad (7)$$

The specific speed and specific diameter are dimensionless parameters and defined by equations (8) and (9) as stated in (Balje, 1981; Moustapha et al., 2003; Dixon and Hall, 2010) as follows:

$$n_s = \frac{\Omega\sqrt{\frac{\dot{m}}{\rho_{exit}}}}{(\Delta h_{is})^{0.75}} \quad (8)$$

$$d_s = \frac{d_{rotor}\,(\Delta h_{is})^{0.25}}{\sqrt{\frac{\dot{m}}{\rho_{exit}}}} \quad (9)$$

The mean diameter is midway point between the tip and the hub and it can be defined as the diameter that divides the annulus into two equal areas as follows (Dixon and Hall, 2010):

$$r_m^2 = \left(r_t^2 + r_h^2\right)/2 \quad (10)$$

The PD code of an AFT is developed based on the AMDCKO (Ainley and Mathieson; Dunham and Came; Kacker and Okapuu) losses model, to calculate the losses through the blade's passage of the AFT. The total losses in terms of profile, secondary flow, tip-leakage and trailing edge losses are used to predict the

performance of the AFT in both single and two stage configurations. The total losses AMDCKO model is expressed in equation (11) (Japikse and Baines, 1994; Moustapha et al., 2003) and outlined in Table 3 as follows:

$$K_T = K_P f_{Re} + K_{Sec} + K_{TE} + K_{TC} \tag{11}$$

The turbine stage total-to-total isentropic efficiency and total-to-static isentropic efficiency in terms of enthalpy loss is as follows (Dixon and Hall, 2010):

$$\eta_{tt} = \frac{1}{1 + \left[\zeta_R w_3^2/2 + \left(\zeta_S C_2^2/2\right)\left(h_3/h_2\right)\right]/(h_{01} - h_{03})} \tag{12}$$

$$\eta_{ts} = \frac{1}{1 + \left[\zeta_R w_3^2/2 + \left(\zeta_S C_2^2/2\right)\left(h_3/h_2\right) + C_3^2/2\right]/(h_{01} - h_{03})} \tag{13}$$

The enthalpy loss and pressure loss coefficients are approximately equal at small values of enthalpy (Japikse and Baines, 1994). The full details of the conversion from the pressure loss to the enthalpy loss are outlined in Moustapha et al. (2003).

Table 3 AMDCKO losses model.

Loss type	Loss correlation	Ref.
Profile loss	$K_P^* = \left\{K_{P(\alpha_{1b}=0)} + \left\|\frac{\alpha_{1b}}{\alpha_2}\right\|\left(\frac{\alpha_{1b}}{\alpha_2}\right)\left[K_{P(\alpha_{1b}=\alpha_2)} - K_{P(\alpha_{1b}=0)}\right]\right\}\left(\frac{t_{max}/c}{0.2}\right)^{(\alpha_{1b}/\alpha_2)}$ $K_P = 0.914\left(\frac{2}{3}K_P^* K_{accel} + K_{sh}\right)$	Japikse and Baines (1994); Moustapha et al. (2003)
Secondary loss	$K_{sec}^* = 0.0334 f_{AS}\left(\frac{\cos\alpha_2}{\cos\alpha_{1b}}\right)\left(\frac{C_L}{S/c}\right)^2\frac{\cos^2\alpha_2}{\cos^3\alpha_m}$	Moustapha et al. (2003)
Trailing Edge loss	$K_{TE} = \frac{\Delta P_0}{0.5\rho C_2^2} = \left(\frac{t_2}{o_2 - t_2}\right)$	Da Lio et al. (2014)
Tip clearance loss	$K_{TC} = 4B\left(\frac{\tau}{h}\right)\frac{\cos^2(\alpha_2)}{\cos(\alpha_m)}(\tan\alpha_1 - \tan\alpha_2)$	Moustapha et al. (2003)

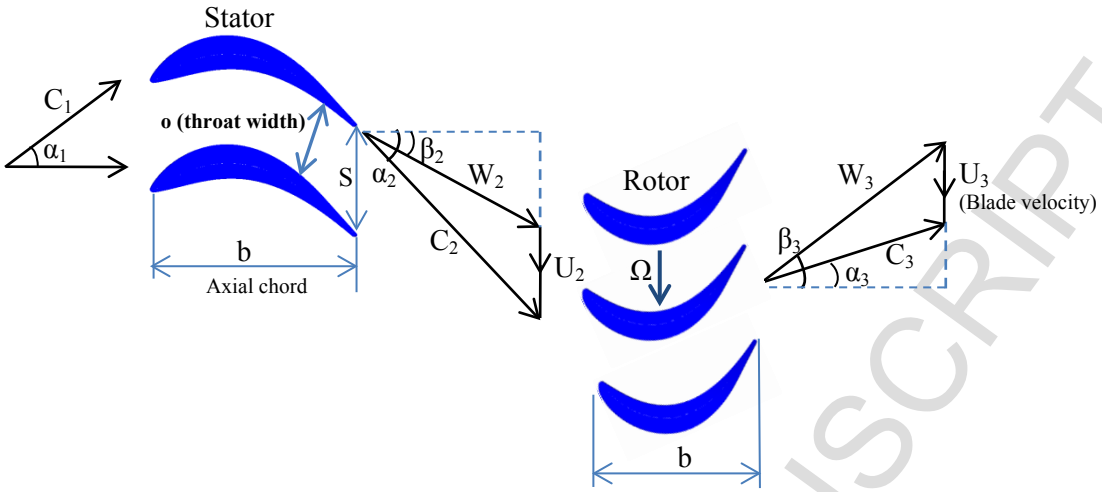

Fig. 3. Schematic of blade passage for both axial and radial out-flow configurations.

3.2 Radial outflow turbine (ROT) design

The specific work in the ROT is low compared with the AFT due to the reduction of the peripheral velocity through the expansion of the working fluid ($U_2 < U_3$) as illustrated in Fig. 3. The losses model of the AFT design (i.e. Table 3) is borrowed and applied in the PD of the radial-outflow turbine. Consequently, the equations (6,11,12,13) and Table 3 are used in the PD code of the ROT configuration. In this configuration, the distribution of the blade along the stage diameter is affected by the blade's height and chord. The outlet section area and the stage diameter are calculated as follows (Casati et al., 2014):

$$A_{out} = H_{out} o = \frac{\dot{m}}{\rho_{out} V_{out} N_{blds}} \quad (14)$$

$$D_{out} = D_{in} + b \quad (15)$$

Assuming a rectilinear suction blade end-side, the relationship between blade geometric discharge angle and outlet width is calculated as:

$$o = S cos\,(BDA) \quad (16)$$

where BDA is a blade geometric discharge angle, equivalent to α_2 and β_3 in Fig. 3.

The blade pitch (S) is calculated based on the following equation:

$$S = {}^{\pi D_{out}}/_{N_{blds}} \quad (17)$$

The blade height is calculated by rearranging equation (14) as:

$$H_{out} = \frac{\dot{m}}{\rho_{out} V_{out} \cos(BDA) D_{out} \pi} \quad (18)$$

3.3 Radial-inflow turbine (RIT) design

Fig. 4 shows the basic geometry of the RIT and rotor geometry that are implemented according to the methodology offered by Whitfield and Baines (1990) and Moustapha et al. (2003). To obtain the best turbine isentropic efficiency, the dimensionless parameters, i.e. the flow and loading coefficients (ϕ, ψ) are essential and given with an inlet blade angle (β_4) of 70° (Whitfield and Baines, 1990). The current losses model of the RIT combines: the incidence, disk friction, friction, secondary, tip clearance, windage, exit energy, nozzle friction and volute losses model, as tabulated in Table 4. The details of the dimensions of the RIT stage calculations are explained in Glassman (1976) and Whitfield and Baines (1990). The total-to-total turbine isentropic efficiency and total-to-static turbine isentropic efficiency are presented in equation (19) as following (Ventura et al., 2012):

$$\eta = \frac{\Delta h_{\text{actual}}}{\Delta h_{\text{actual}} + \sum(\Delta h_{\text{total losses}})} \quad (19)$$

Table 4 RIT losses modeling.

Type of losses	Correlation	Ref.
Incidence loss	$\Delta h_{incidence} = \frac{w_{\theta 4}^2}{2}$	Ventura et al. (2012)
Disk friction loss	$\Delta h_{disk\ friction} = \frac{k_f \rho U_4^3 r_4^2}{4\dot{m}}$	Whitfield and Baines (1990)
Friction loss	$\Delta h_{friction} = f_{curve}\left[\frac{w_4 + \left(\frac{w_{5tip} + w_{5hub}}{2}\right)}{2}\right]\frac{l_{hyd}}{d_{hyd}}$	Suhrmann et al. (2010)
Secondary loss	$\Delta h_{secondary} = \frac{C_4^2 . d_4}{Z_{rotor} . r_c}$	Suhrmann et al. (2010)
Tip clearance loss	$\Delta h_{tip\ clerance} = \frac{U_4^3 . Z_{rotor}}{8\pi}\left(0.4.\varepsilon_x.C_x + 0.75.\varepsilon_r.C_r - 0.3\sqrt{}\right.$	Japikse and Baines (1994)
Windage loss	$\Delta h_{windage} = k_f \frac{\overline{\rho} . U_4^3 r_4^2}{2 . \dot{m} . w_5^2}$	Moustapha et al. (2003), Ventura et al. (2012)
Exit energy loss	$\Delta h_{exit} = 0.5 C_5^2$	Suhrmann et al. (2010)
Nozzle friction loss	$\Delta h_{friction} = 4 . f_{nozzle} . \overline{C} \frac{l_{hyd}}{d_{hyd}}$	Whitfield and Baines (1990)
Volute loss	$\Delta h_{volute\ loss} = \frac{K_{volute} C_2^2}{2}$	Whitfield and Baines (1990)

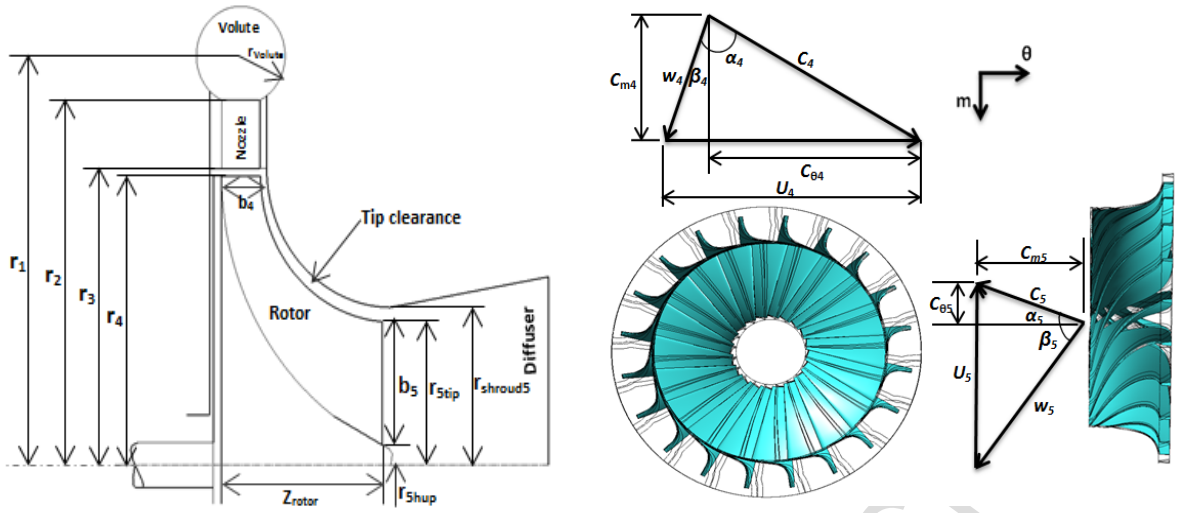

Fig. 4. Cross section of RIT stage (left), velocity triangles of RIT at the rotor inlet and outlet (right) (Al Jubori et al., 2016).

3.4 Input and output from the preliminary mean-line design (PD)

The main target of the PD for each turbine's configuration is to deliver the velocity triangles and flow angles based on the dimensionless parameters (i.e. flow coefficient ϕ, loading coefficient ψ and reaction R_n) to determine the initial blade shape, turbine size and performance. The losses correlation model for each configuration is used to calculate the new isentropic efficiency that it is compared to the initial estimated value. The PD mathematical model was developed and solved using the Engineering Equation Solver (EES); the PD methodology procedure is shown in Fig. 5. The flow chart in Fig. 5 indicated that the PD is a highly iterative procedure of turbine design and hence, comprehensive studies are required for different configurations, based on various input parameters. The EES code of the PD is capable of predicting the turbine's geometry and performance for each configuration including; the input parameters, working fluids and operating conditions are as tabulated in Table 5. The PD methodology outputs are outlined in Table 6 for each turbine configuration.

Table 5 The PD code input parameters for all turbines configurations and their ranges/values.

Flow and dimension Parameter	Unit	Values/Ranges
Flow coefficient (ϕ)	-	0.2-1.0
Loading coefficient (Ψ)	-	0.6-1.4
Reaction (R_n)	-	0.4-0.6
Hub/tip radius ratio (r_h/r_t)	-	0.5-0.75
Inlet to outlet radius ratio of the RIT nozzle (r_2/r_3)	-	1.25-1.35
Outlet hub to inlet radius ratio of the RIT rotor (r_{5hub}/r_4)	-	0.6-0.8
Blade speed ratio	-	0.7
Rotor RIT exit absolute flow angle (α_5)	degree	0.0
Operating conditions		
Inlet total temperature	K	365
Inlet total pressure	bar	Corresponding saturated vapour pressure at inlet temperature
Rotational speed	rpm	18000-45000
Degree of superheating	K	0-5

Working fluid mass flow rate	kg/s	0.1 – 0.5
Organic fluids	-	R141b, R245fa, isopentane

Table 6 The PD code output for all turbines configurations for $\dot{m} = 0.5$ kg/s and three selected working fluids.

Parameters	Working fluid		
	R141b	R245fa	isopentane
Axial turbine			
Blade height (H) mm	9.597	8.775	10.25
Tip diameter (d_t) mm	60.51	58.150	63.120
Hub diameter (d_h) mm	41.315	40.600	42.620
TE blade thickness (mm)	0.3	0.3	0.3
Tip clearance (mm)	0.35	0.35	0.35
LE Blade Angle (deg)	-12.45	-16.38	-20.17
TE Blade Angle (deg)	67.12	65.65	69.41
Stagger angle (deg)	35.82	33.67	38.93
Solidity (c/S) (-)	1.847	1.715	1.936
Z_{stator} (-)	23	21	23
Z_{rotor} (-)	22	20	22
Turbine isentropic Efficiency (%)	82.57	84.16	81.31
Power output (kW)	9.036	10.408	8.411
Radial-outflow			
Blade height (H) (mm)	10.963	10.160	11.948
Outlet diameter (D_{out}) (mm)	88.147	82.672	95.450
Inlet diameter (D_{in}) (mm)	49.438	46.342	52.627
TE blade thickness (mm)	0.3	0.3	0.3
Tip clearance (mm)	0.35	0.35	0.35
LE Blade Angle (deg)	-17.685	-14.015	-20.173
TE Blade Angle (deg)	66.941	64.360	68.167
Stagger angle (deg)	30.135	28.048	32.615
Solidity (c/S) (-)	1.916	1.825	1.985
Z_{stator} (-)	27	25	29
Z_{rotor} (-)	42	40	44
Turbine isentropic Efficiency (%)	79.47	81.42	77.91
Power output (kW)	8.561	9.685	7.753
Radial-inflow			
α_4 (degree)	73.05	69.77	77.76
β_4	45.59	40.29	49.16
$\beta_{blade,4}$	65.59	60.29	69.16
$\beta_{tip,5}$	-61.49	-57.61	-64.58
$\beta_{hub,5}$	-50.65	-46.47	-56.51
d_1 (mm)	88.139	80.625	97.346
d_2 (mm)	81.867	74.349	90.765
d_3 (mm)	71.546	65.276	80.887
d_4 (mm)	69.546	63.276	77.887
d_{5tip} (mm)	36.623	33.251	40.909
d_{5hub} (mm)	17.536	14.131	19.285
b_4 (mm)	3.013	2.785	3.647
Z_{nozzle} (-)	29	25	41
Z_{rotor} (-)	18	16	20
Turbine isentropic Efficiency (%)	82.85	85.01	81.64
Power output (kW)	9.318	11.172	8.959

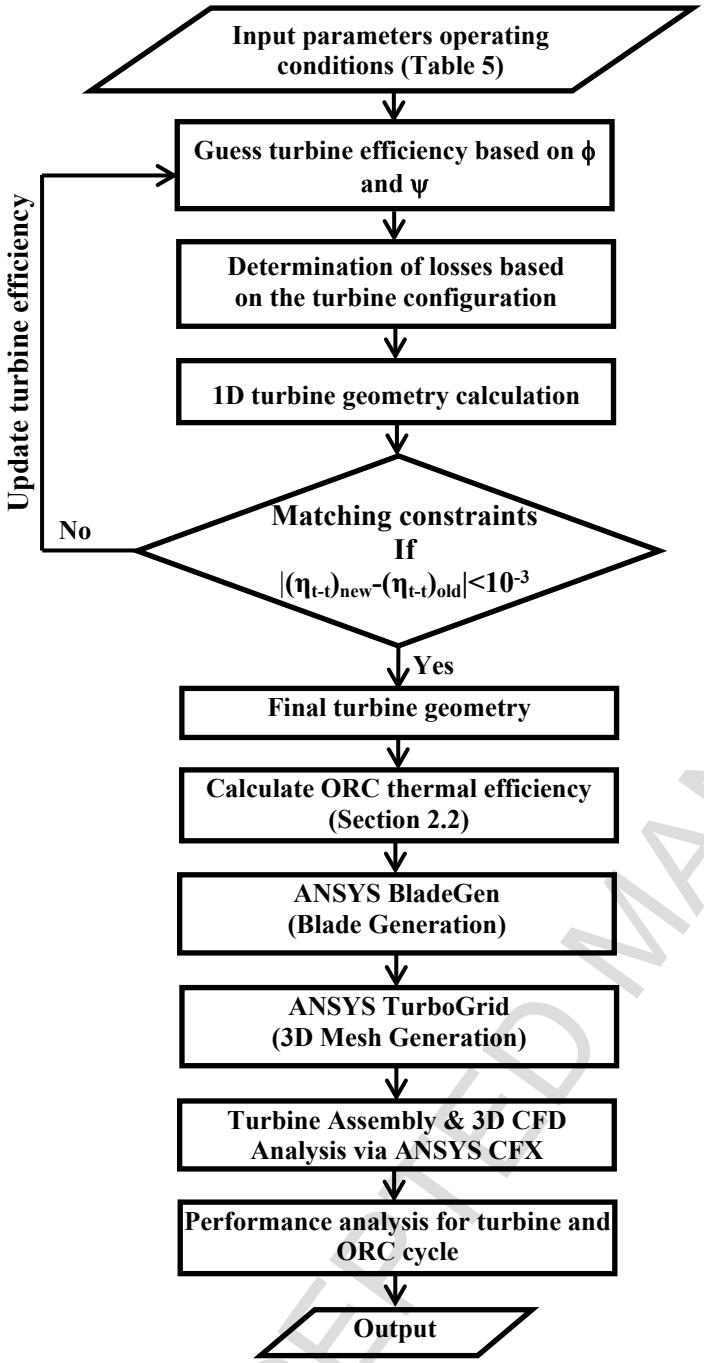

Fig. 5 The flow chart of turbine PD methodology procedure.

4. Three-dimensional CFD methodology

CFD analysis is considered as one of the critical analysis techniques, hand-in-hand with the PD model to predict the accurate aerodynamics' performance maps of the turbines, operating with three organic fluids, namely (R141b, R245fa and isopentane). The ANSYS®17 software is utilized to implement the 3D CFD simulation throughout the turbine stage (stator-rotor blade passage). The principle blade geometry and turbine dimensions delivered for the stator and rotor are imported into the ANSYS®17 tool as the blade design module, to generate the stator and rotor blade geometry for each turbine configuration stage, as illustrated in Fig. 6.

The angle/thickness and pressure/suction modes are used to define the hub, shroud and blade profile curves for both stator and rotor blades. The ANSYS®17-Turbo Grid is employed to create the computational grid of the flow domain across the blade passages of the stator and rotor, via hexahedral mesh based on the O-H grid. ATM Optimized (Automatic Topology and Meshing) has been applied to allow the Turbo-Grid to determine an appropriate topology for the blade passage according to the blade angle, the leading edge and the trailing edge type. The grid independence studies of each turbine configuration and working fluids were carried out to ensure that the results of 3D CFD analysis are meshing independent. The computational meshes were clustered and then the simulation re-run and repeated until the mesh independent solution was reached for each turbine configuration and working fluid. Fig. 7 shows the grid independence study for each turbine configuration with R245fa as the working fluid, where the solution becomes grid-independent by the number of nodes above those listed in Table 7. While Fig. 8 shows the mesh density of the blade-to-blade passage for each turbine configuration.

The 3D CFD simulations are conducted by solving RANS equations combined with the k-ω/SST (shear stress transport) turbulence model through the ANSYS®17-CFX. The k-ω/SST turbulence model has the ability to capture the turbulence closure based on automatic wall-function treatment by identifying the non-dimensional distance (y^+) of the first node after the node's wall; where the y^+ is kept equal to one or less than unity as recommended in the CFX user's manual. The transport equations of the k-ω turbulence model used to calculate the turbulent kinetic energy and the specific dissipation rate are as follows:

$$\frac{\partial}{\partial t}(\rho k) + \frac{\partial}{\partial x_i}(\rho k u_i) = \frac{\partial}{\partial x_j}\left(\Gamma_k \frac{\partial k}{\partial x_j}\right) + G_k - Y_k + S_K \quad (20)$$

$$\frac{\partial}{\partial t}(\rho \omega) + \frac{\partial}{\partial x_i}(\rho \omega u_i) = \frac{\partial}{\partial x_j}\left(\Gamma_k \frac{\partial \omega}{\partial x_j}\right) + G_\omega - Y_\omega + S_\omega \quad (21)$$

where G_k and G_ω represent the generation of turbulent kinetic energy and its dissipation rate; Y_k and Y_ω represent the fluctuating dilation in compressible turbulence; S_k and S_ω are the source terms of the k-ω turbulence model.

A mixing plane interface was applied at the turbine stage interface (i.e. stator and rotor) to provide the communication through the stationary and rotating domain of the blade rows. The GGI (i.e. Generalised Grid Interface) feature was used with steady state flow and stage analysis. All CFD simulations were carried out under steady state flow condition with convergence criterion of 10^{-5} for all residuals (RMS) values and a time scale of 0.5/Ω as recommended in the CFX user's manual. The inlet's total pressure and temperature were fixed at the turbine stage inlet while the static pressure was specified at the turbine stage outlet (i.e. rotor outlet);

turbulence intensity of 5% was specified at the inlet as suggested in the CFX user's manual. In all CFD analyses, the condition of walls was considered to be smooth, non-slip and adiabatic. The REFPROP software working fluids' database was integrated with the ANSYS®17-CFX database to deliver an accurate thermodynamic properties model of the working fluids' properties for the CFD analyses. All 3D CFD simulations of the whole turbine stage were conducted using an Intel® CPU core i7 – 4820K@ 3.70 GHz with 48 GB RAM memory run in parallel with 4 CPU cores.

Table 7 Summary of the size of grid independence for each turbine configuration.

Turbine Configuration	1st Stator No. of Nodes	1st Rotor No. of Nodes	2nd Stator No. of Nodes	2nd Rotor No. of Nodes
Single-stage axial turbine	455000	570000	-	-
Single-stage radial-inflow turbine	490000	615000	-	-
Single-stage radial-outflow turbine	465000	600000	-	-
Two-stage axial turbine	460000	580000	470000	590000
Two-stage radial-outflow turbine	450000	600000	470000	600000

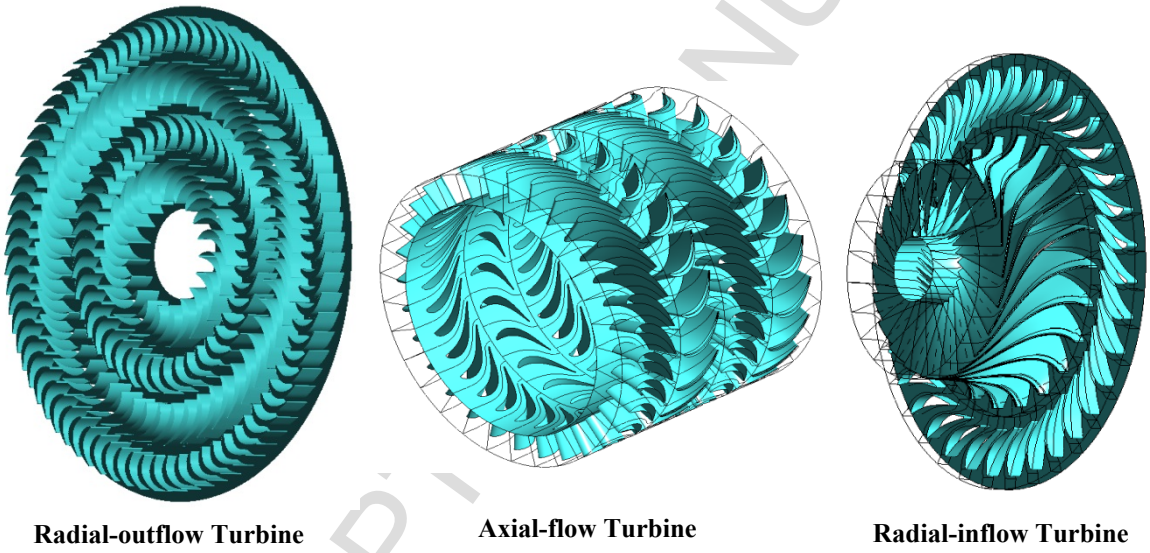

Radial-outflow Turbine **Axial-flow Turbine** **Radial-inflow Turbine**

Fig. 6. 3D views of each turbine configuration.

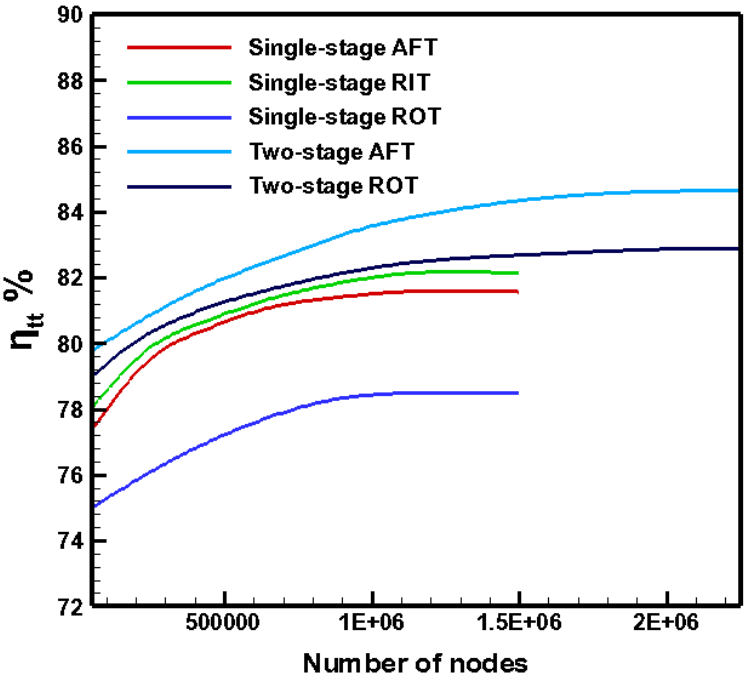

Fig. 7. Grid sensitivity based on the turbine isentropic efficiency for all turbines' configurations with R245fa as the working fluid.

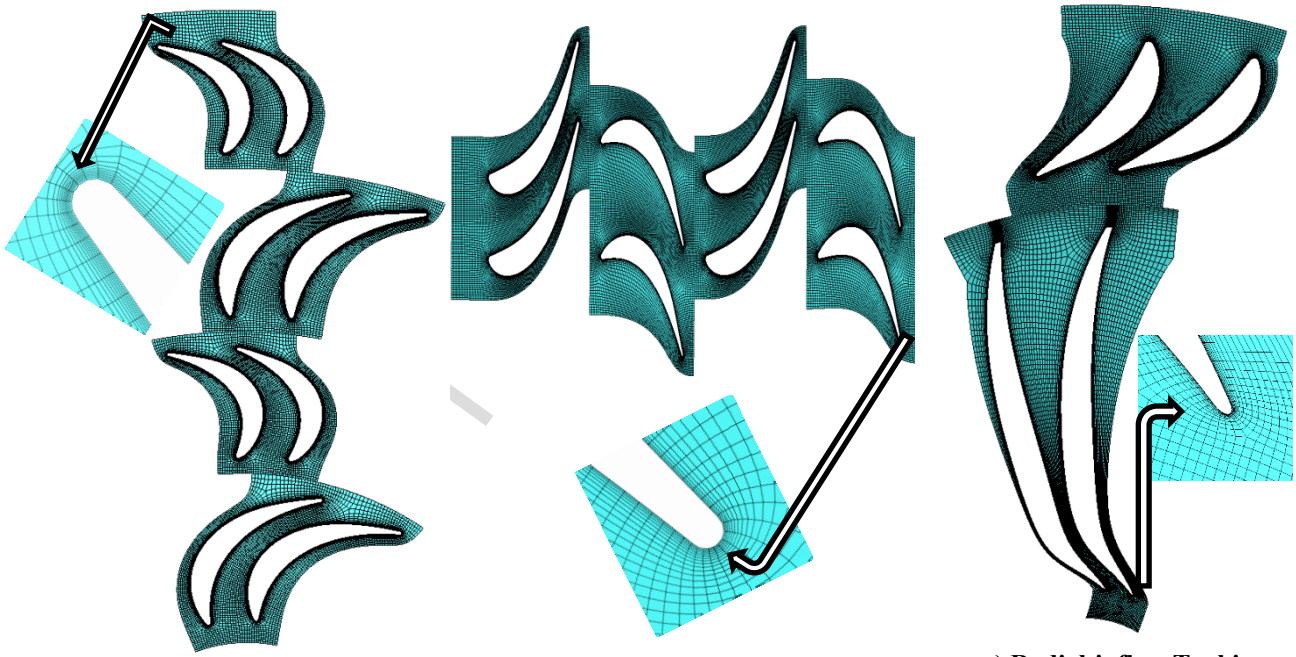

a) Radial-outflow Turbine **b) Axial-flow Turbine** **c) Radial-inflow Turbine**

Fig. 8. Mesh density for blade-to-blade passage stage of three turbines configurations.

5. CFD verification and validation

The developed PD defined in section 3 for each turbine configuration is validated against the published benchmark cases, namely the Glassman cases (codes) as detailed in Glassman (1992) and Glassman (1995) for single-stage axial and radial-inflow turbine configurations respectively. The PD results of the global

performance parameters (i.e. turbine efficiency and power) are in good agreement with the Glassman cases and the maximum variation are within the acceptable margin as demonstrated in Fig. 9 for all working fluids.

Due to the lack of availability in the experimental data for small-scale ORC turbines, verification of the present 3D CFD model for each turbine configuration is made against the PD results at nominal operating conditions (i.e. Table 5), as shown in Fig. 9a and b. The turbine efficiency and power are evaluated for five turbine configurations with working fluid R245fa. The comparison results exhibited that the maximum variation between the PD and CFD results was 3.28%, 3.56%, 3.85%, 3.65% and 4.12% for single-stage AFT, RIT, ROT and two-stage AFT and ROT respectively. The variance between the PD and CFD is mostly because of the characteristic of the 1D mean-line design, which is not able to provide all 3D flow characteristics. Eventually, there was better agreement between these results than can be seen in Fiaschi et al. (2016) and Russell et al. (2016), in which there was a 6-9% deviation in terms of the turbine isentropic efficiency.

Furthermore, the 3D CFD results of the single-stage RIT and two-stage AFT turbines are compared with experimental data available in Jones (1996) and Kofskey and Nusbaum (1968), as shown in Figs. 10 and 11 respectively. To allow a fair comparison, most of the range/values of dimensions and operating conditions are taken from the above-mentioned references, as shown in Table 8 for radial inflow turbine and Table 9 for axial flow turbine respectively. The comparison results showed that the maximum difference in efficiency was about 4.29% with single-stage RIT configuration as shown in Fig. 10, compared to 3.57% with two-stage AFT as shown in Fig.11. This difference could also be attributed to the complex phenomena that can be accurately handled by 3D CFD modelling.

Table 8 Details of the radial-inflow turbine geometry of a real case (Jones case (Jones, 1996)).

Parameters	Value	Parameters	Value
r_2 (m)	0.074	β_4 (degree)	31.8
r_3 (m)	0.0635	β_5 (degree)	-57.40
r_4 (m)	0.0582	Z_{nozzle} (-)	19
r_{5tip} (m)	0.0368	Z_{rotor} (-)	16
r_{5hup} (m)	0.0152	Nozzle chord(m)	0.0229
b_4 (m)	0.00618	Rotor chord (m)	0.0457
b_5 (m)	0.00635	Radial Clearance (m)	0.23×10^{-3}
α_3 (degree)	77.80	Nozzle trailing edge thickness (m)	0.51×10^{-3}
α_4 (degree)	76.8	Rotor trailing edge thickness (m)	0.76×10^{-3}
α_5 (degree)	-0.03		

Table 9 Input parameters and two-stage geometry for Kofskey and Nusbaum (1968).

Input parameters		**Turbine geometry**	
Property	***Value***	***Property***	***Value***
Working fluid (-)	Argon	Rotor number of blades (-)	36
Inlet total pressure (bar)	1.5826 bar	Stator number of blades (-)	44, 40
Inlet total temperature (K)	936.11 K	Tip diameter (mm)	246, 249
Mass flow rate (kg/s)	0.277	Mean diameter (mm)	215.9
Total–to-total pressure ratio (-)	1.226	Tip clearance (mm)	0.3, 0.38
Total–to-static pressure ratio (-)	1.232	Inlet flow angle (degree)	12
Flow coefficient (-)	0.465-0.651	Stator solidity (-)	1.57, 1.56
Rotational speed (rpm)	12000 rpm	Rotor solidity (-)	1.3, 1.4

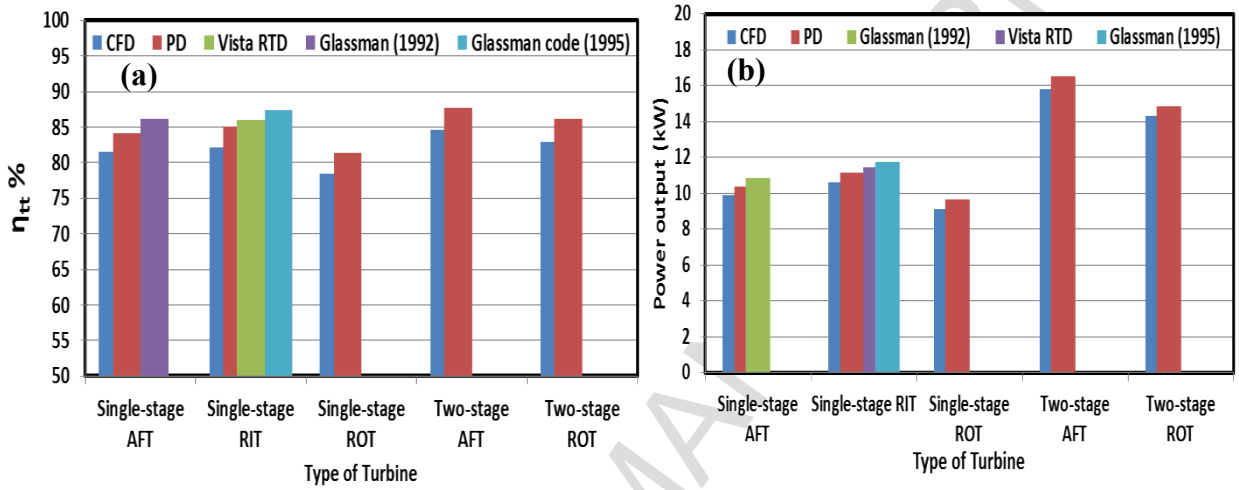

Fig. 9. Comparison the current PD models with Glassman codes and CFD for each turbine configuration with R245fa as the working fluid in terms of power and efficiency.

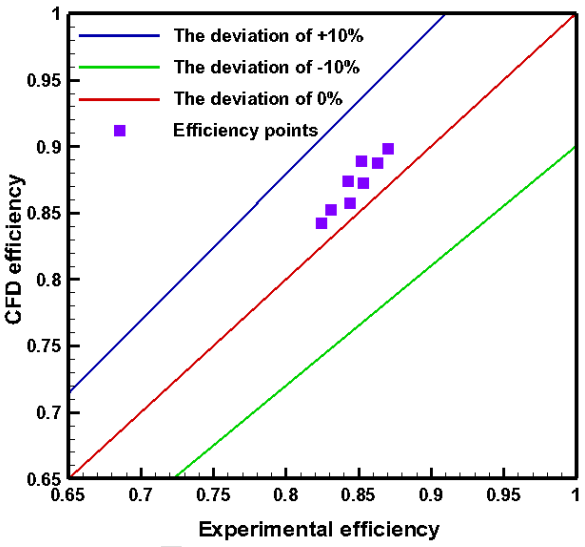

Fig. 10. Comparison of the CFD efficiency with experimental efficiency for Jones (1996) for RIT turbine.

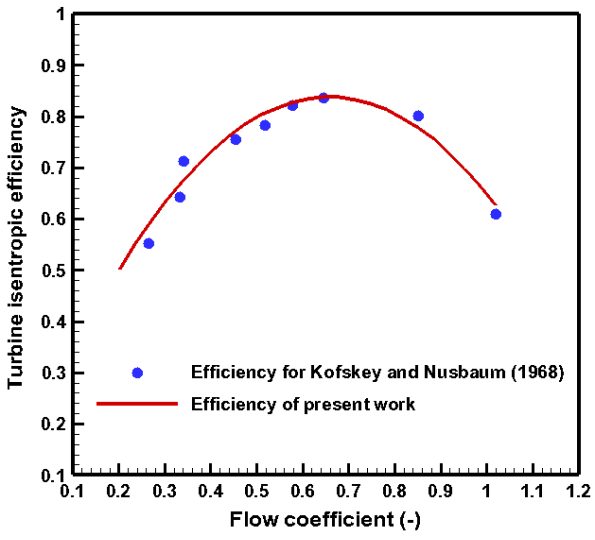

Fig. 11. Comparison of the 3D CFD results from current model with Kofskey and Nusbaum (1968)

6. CFD results

The turbine isentropic efficiency and power output as a global performance for five turbine configurations (i.e. single-stage axial, radial-inflow, radial-outflow and two-stage axial and radial-out flow turbines) are sensitive to expansion ratio, mass flow rate, specific speed, and turbine size in terms of specific diameter at nominal design conditions (i.e. Table 5) and off-design conditions, as displayed in Figs. 12-16 as parametric analyses. These configurations are investigated based on the 3D CFD analysis in order to explore which delivers the best turbine performance leading to high thermal system efficiency under available operating conditions with three organic working fluids.

It is evident from Fig. 12a,b that the two-stage axial and radial-outflow turbine configurations have a considerably higher overall turbine isentropic efficiency and power output at an expansion ratio of about 6.0; where the expansion ratio is defined based on the pressure ratio. It is also clear from Fig. 12a,b that the maximum overall efficiency of the two-stage axial and radial-outflow turbines was 84.64% and 82.90% respectively; compared with 81.55% and 78.48% for the single-stage configuration with R245fa as the working fluid. For all single-stage turbine configurations, the reduction in turbine isentropic efficiency at a high-pressure ratio is due to the probability of chocking, which occurs at a large expansion ratio when the turbine stage runs at off-design points. It is clear from Fig. 12b that the maximum total power output from the two-stage turbine configuration is considerably higher than the single-stage configuration for all types of turbine; where the maximum provided power output from the two-stage configuration was 15.798 kW and 14.331 kW for axial and radial-outflow turbines respectively, with the working fluid R245fa.

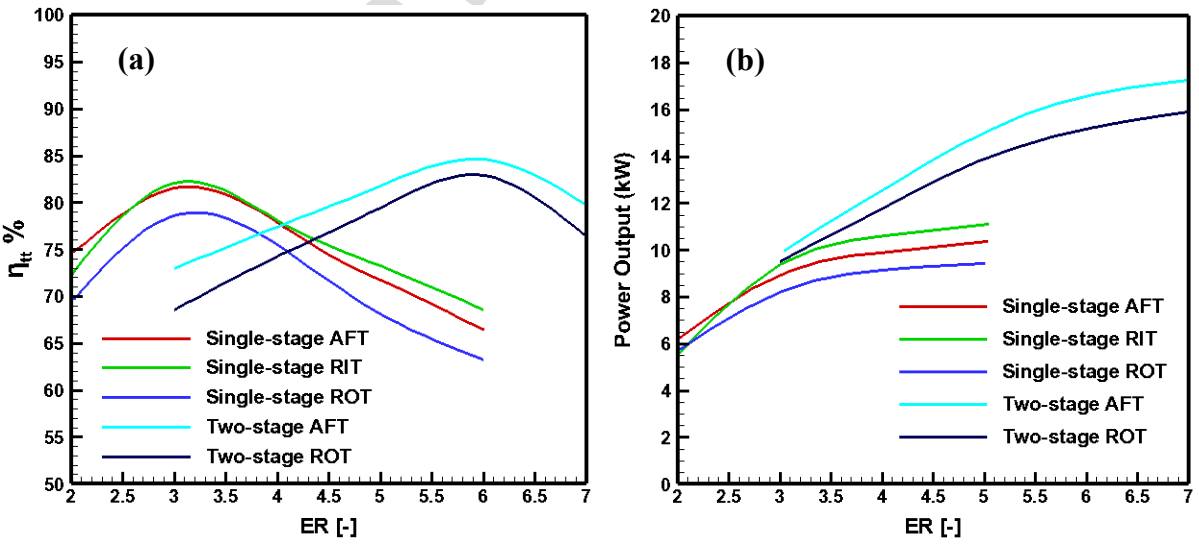

Fig.12. Variation of the turbine isentropic efficiency (a) and power (b) with expansion ratio for all turbines configurations at $\dot{m} = 0.5\ kg/s$ with R245fa working fluids.

Fig. 13a,b illustrate the change of the turbine overall isentropic efficiency and power output with the mass flow rate for all turbines' configurations at design conditions (i.e. Table 5). It is depicted from this figure that the overall isentropic efficiency and power increase as the mass flow rates increase, with R245fa as a working fluid. Power output here is considered as the relationship between the mass flow rate and the enthalpy drop. As the working fluid mass flow rate increases the actual enthalpy drops, but the power output increases; this in turn leads to larger turbine isentropic efficiency as seen in Fig. 13a,b. By increasing the mass flow rate a larger blade height is achieved, which leads to a reduction in the blade tip clearance losses and possibly, other losses (e.g. secondary loss) as well.

It is evident from Fig. 13a that the minimum turbine efficiency was 66.13% for the single-stage radial-outflow turbine, compared with about 71.72% for the single-stage radial-inflow turbine at a mass flow rate of 0.1 kg/s working with R245fa. While the two-stage axial and radial-outflow turbines have the maximum turbine isentropic efficiency and power output at a mass flow rate of 0.5 kg/s.

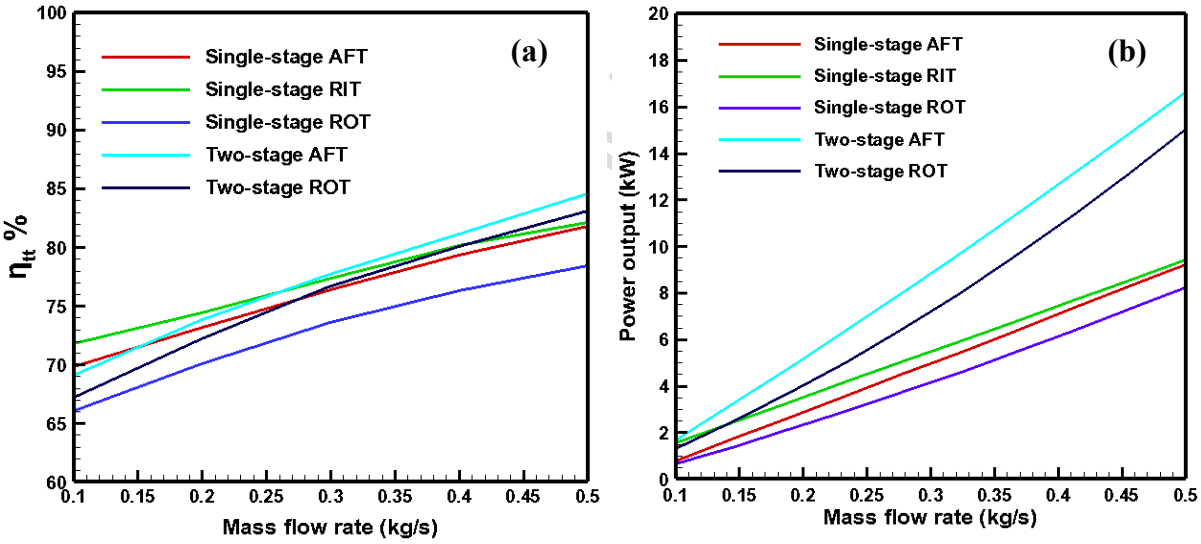

Fig.13. Variation of the turbine efficiency (a) and power (b) with mass flow rate for all turbines configurations with R245fa working fluid.

As shown in Fig. 14a,b at the design point of the rotational speed range of (18000-25000 rpm) for axial and radial-outflow turbines, and at 45000 rpm for the radial-inflow turbine, it harvests the highest overall turbine isentropic efficiency and power. It is clear from Fig. 14a and b, with increasing the rotational speed, the turbine performance (efficiency and power) enhanced and reached the optimum values of power and efficiency at the nominal operating condition (Table 5). Furthermore, it is evident that turbine performance for all turbine configurations is a strong function of rotational speed; as seen when decreasing/increasing the rotational speed from the design point, as an off-design condition at mass flow rate of 0.5 kg/s with the working fluid R245fa.

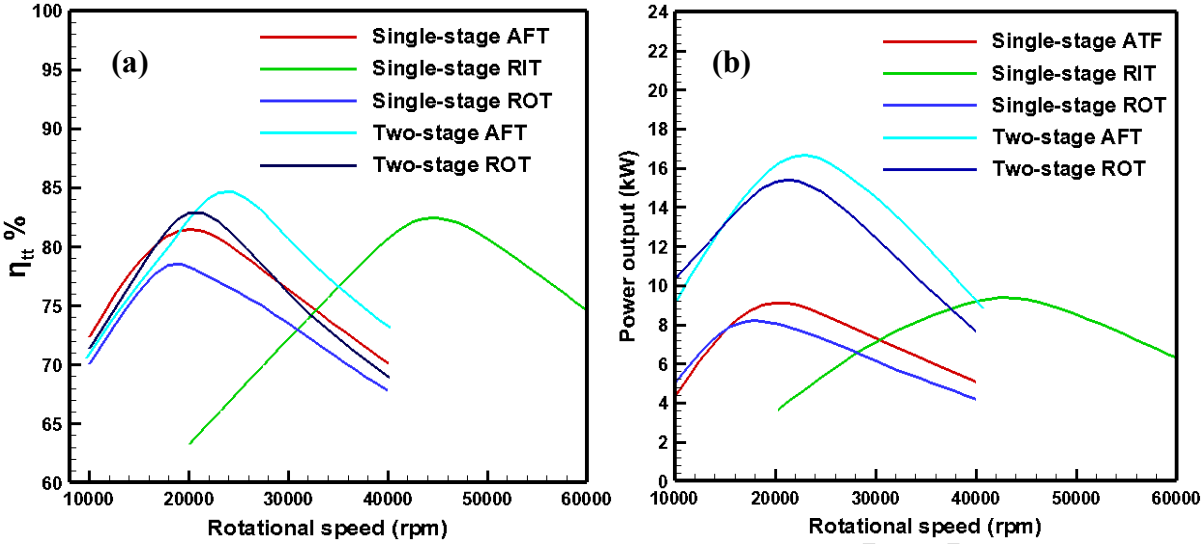

Fig. 14. Variation of turbine efficiency (a), and power (b) with rotational speed for all turbines' configurations with R245fa working fluid.

The optimum specific speeds of all the turbines' configurations at the design point of the pressure ratio and rotational speed with the range of mass flow rates of (0.1-0.5 kg/s) and R245fa as a working fluid are shown in Fig. 15a,b. Based on the definition of the specific speed, i.e. equation (8), the optimum specific speed is dependent on three different parameters, namely rotational speed, mass flow rate and specific work for each turbine configuration. While Fig. 16a,b shows the effect of the turbine size in terms of specific diameter on the turbine efficiency and power respectively, with R245fa as a working fluid. Based on equation (9), the specific diameter depends on the turbine diameter, specific isentropic work and mass flow rate.

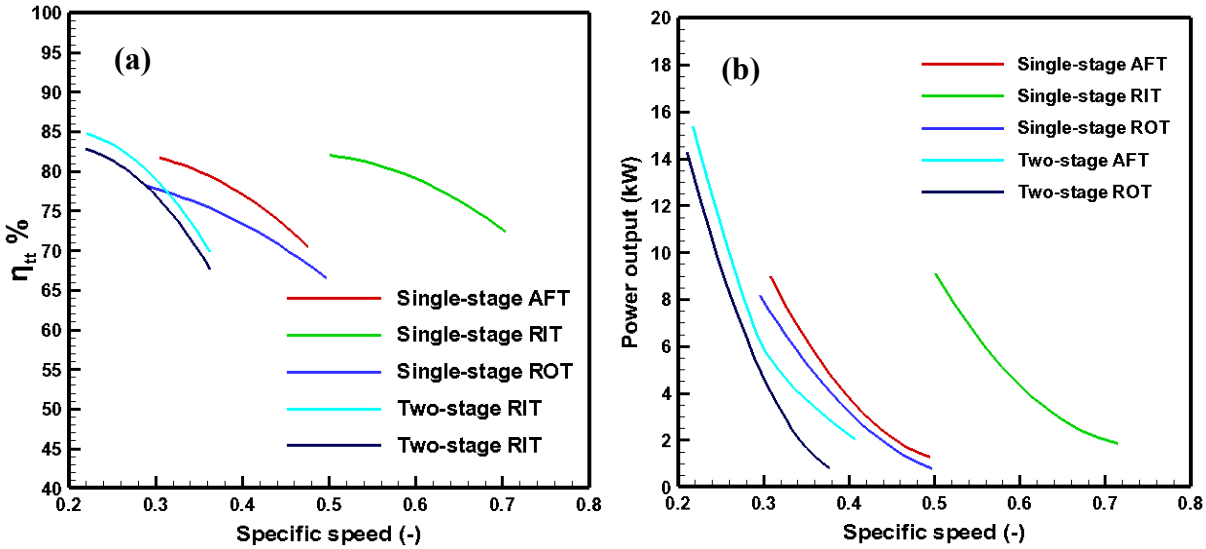

Fig. 15. Variation of turbine efficiency (a) and power (b) with specific speed for all turbines' configurations with R245fa working fluid.

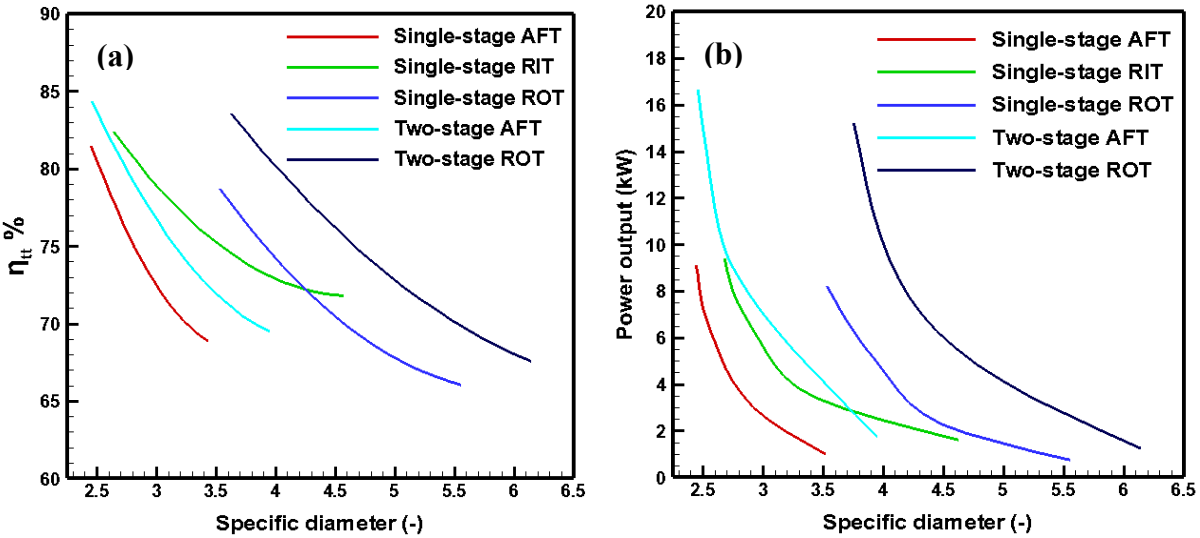

Fig. 16. Variation of the turbine efficiency (a) and power (b) with specific diameter for all turbines' configurations with R245fa working fluid.

Fig. 17a,b presents the evaluation of the turbines' performance (efficiency and power) at nominal conditions for different turbine configurations at the design point (i.e. Table 5). It is obvious that the two-stage configuration of the axial and radial-outflow turbines delivers a high turbine performance (efficiency and power) compared to the single-stage turbine configuration with the working fluid R245fa. The radial-outflow turbine in a single-stage configuration displays a lower performance. The mapping of the working fluids, namely R245fa, R141b and isopentane is presented in Fig. 18a and b for all turbine configurations. It can be seen that R245fa exhibit higher performance compared to R141b and isopentane, due to its large molecular weight working at high expansion ratio and rotational speed with the working fluid mass flow rate of 0.5 kg/s.

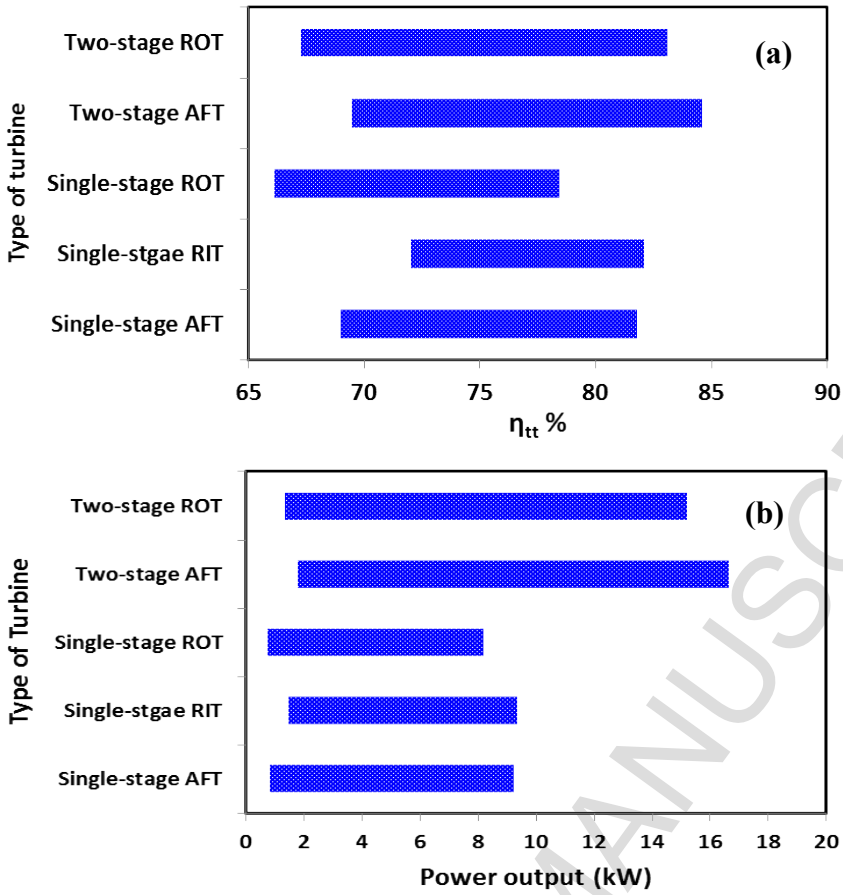

Fig. 17. The range of turbine isentropic efficiency (a), and power (b) for each turbine configuration with R245fa working fluid.

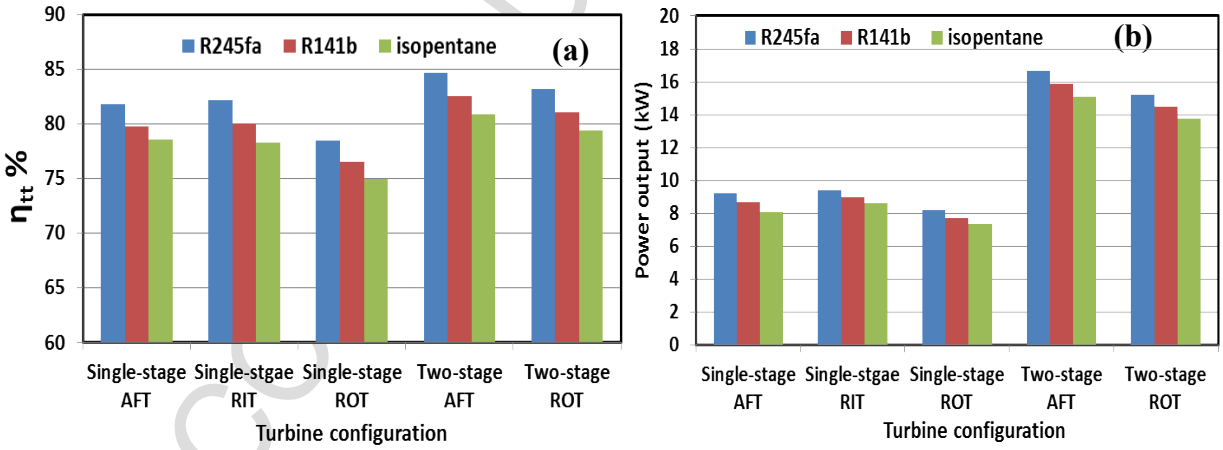

Fig.18. Evaluation of turbine performance for all turbines configurations with three working fluids.

Fig. 19 displays the contour of pressure at mid span (i.e. 50%). It is noticeable that the maximum pressure is at the inlet of the stator of the first stage, as shown in Fig. 19 for three organic working fluids.

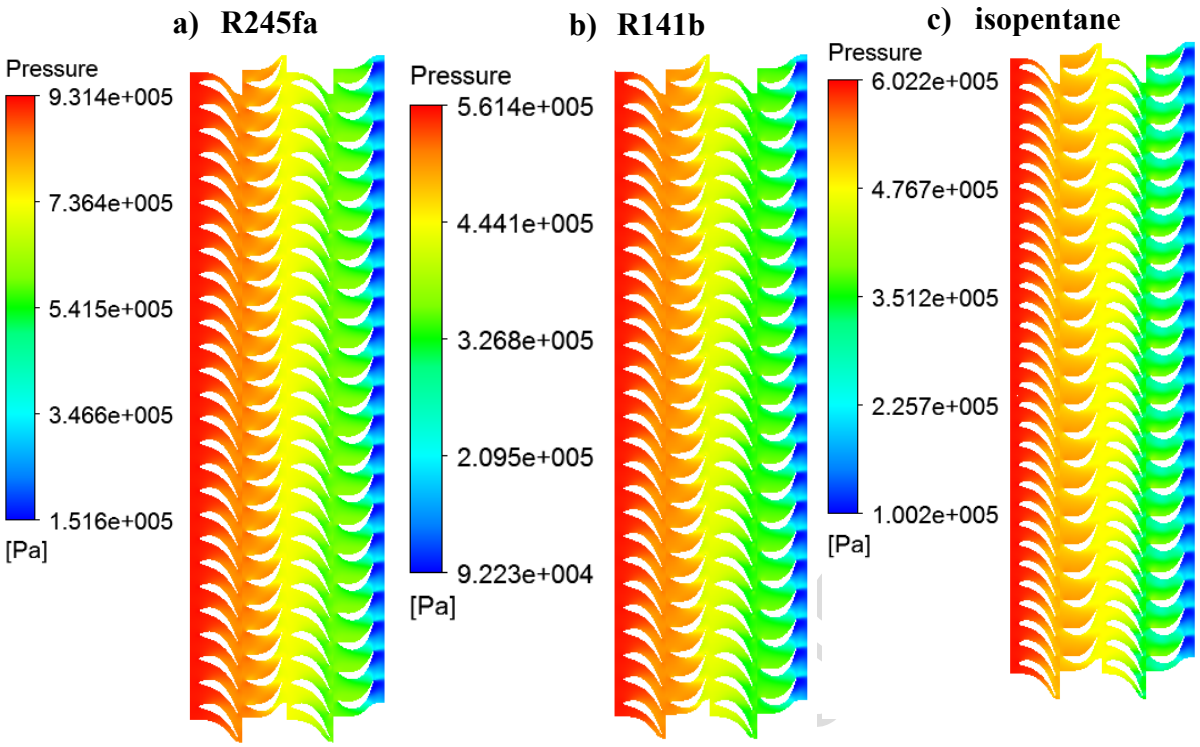

Fig. 19. Pressure distribution contour for two-stage axial turbine configuration for three working fluids.

7. ORC system results

The global performance of the turbine in terms of isentropic efficiency and power output, delivered from 3D CFD analysis for each turbine configuration and working fluid at nominal operating conditions (Table 2), are inserted as input parameters in the ORC system modelling (i.e. equations 1-5) to obtain an accurate ORC system performance in terms of the ORC's thermal efficiency, as shown in Figs. 20 and 21. The turbine performance (efficiency and power) is dynamically obtained based on the PD model and then by 3D CFD analysis with thermodynamic operating conditions for each working fluid. As shown in Fig. 20, the maximum ORC thermal efficiency was from the two-stage axial and radial-outflow turbine configuration with values of 13.96% and 12.80%, compared to 10.39%, 10.75% and 9.84% for the single-stage axial, radial-inflow and radial- outflow configurations with the working fluid R245fa. It is evident that increasing the mass flow rate and inlet temperature of the working fluid leads to an increase in the ORC system's thermal efficiency.

In all turbine configurations, a higher ORC thermal efficiency was achieved with an increase in the mass flow rate of the working fluid; which leads to an increase in the power output from the turbine. Fig. 21a,b depicts that R245fa has the best ORC system performance in terms of thermal cycle efficiency for all turbine configurations, compared with R141b and isopentane at the operating design conditions from Table 5. The evaluation of the second law efficiency for the ORC is revealed in Fig. 21b at nominal design conditions (Table

2) and for all turbine configurations with three organic working fluids. The maximum second law efficiency was 76.05% and 70.73% for the two-stage axial and radial-outflow turbine configurations respectively, with R245fa as a working fluid.

According to these results, the two-stage configuration for axial and radial-outflow turbines is better than shown in other studies (Pei et al., 2011; Kang, 2012; Hu et al., 2015; Kang, 2016); giving a maximum ORC thermal efficiency of about 9.8%, based on a two-stage radial-inflow turbine with an expansion ratio of 11.6 and a mass flow rate of 1.52 kg/s, as reported in Kang (2016). This highlights the potential of this integrated approach, for further accurate prediction of the ORC performance using small-scale single-stage axial, radial-inflow and radial-outflow turbines and two-stage configurations for axial and radial-outflow turbines powered by a low-grade temperature heat source.

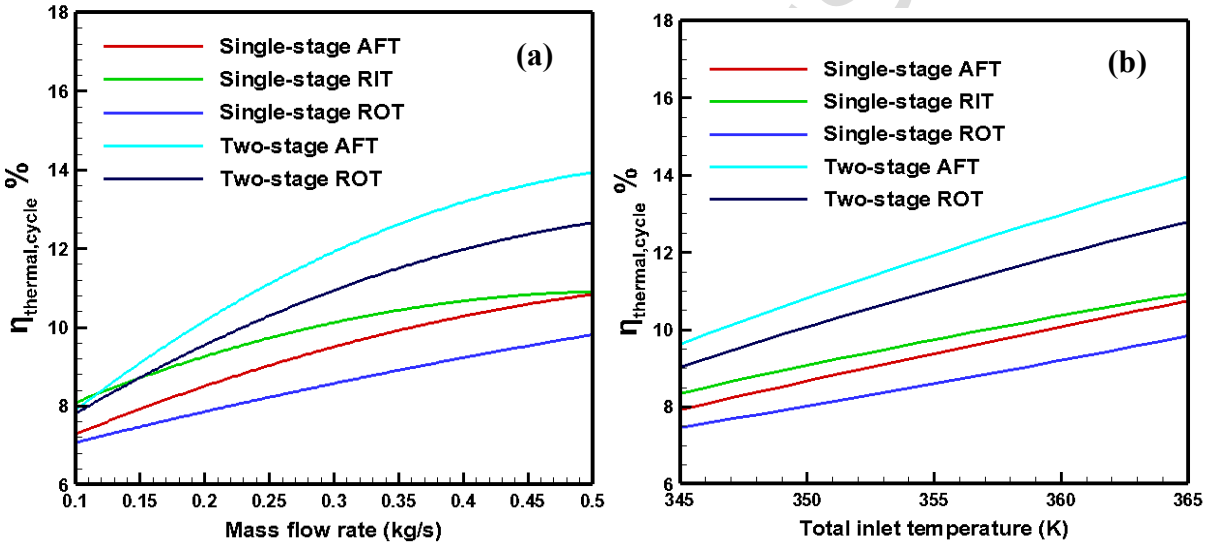

Fig. 20. ORC thermal efficiency with different mass flow rates (a) and turbine total inlet temperature (b) for all turbine configurations.

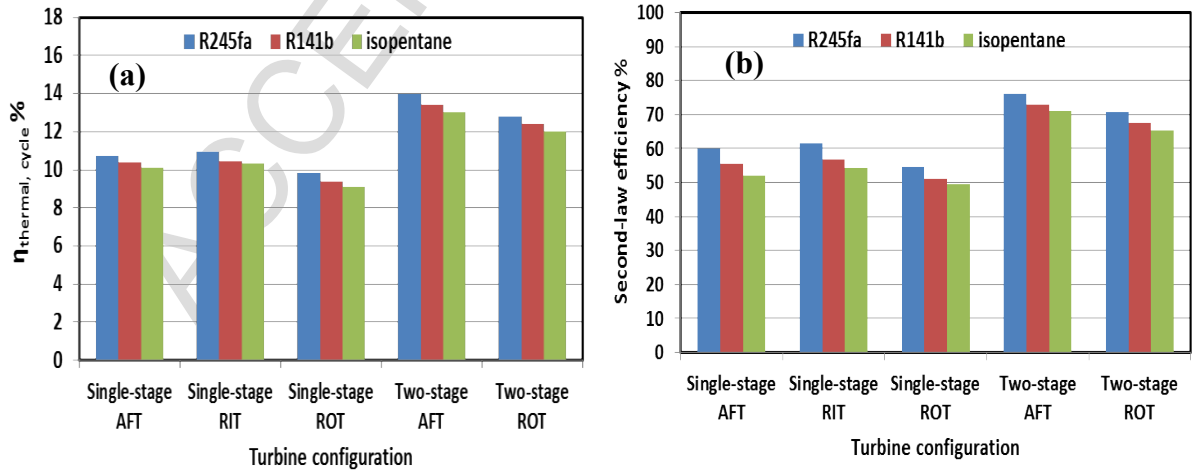

Fig. 21. Cycle thermal efficiency (a); and second law efficiency (b); for all turbine configurations with three working fluids.

8. Conclusions

This work developed a novel, efficient, small-scale single and two-stage configurations for axial, radial-inflow and outflow turbines for a low-temperature heat source and low-power ORC system (<20 kW). In this paper, new performance maps for different small-scale turbine configurations were delivered based on the integrated methodology of the PD, 3D CFD analysis and ORC modelling using REFPROP and real gas formulations of the three working fluids used. The turbine performance maps were generated for different turbine configurations, including single and two stages.

The results exhibited that the configurations of the two-stage axial and radial-outflow turbines showed a considerably higher turbine performance compared to the single-stage configuration at high pressure ratio. The maximum overall isentropic efficiency and power output of the two-stage configuration for the axial and radial-outflow turbines was 84.64% and 15.798 kW for the axial turbine and 82.90% and 14.331 kW for the radial-outflow turbine, with the working fluid R245fa. The maximum ORC thermal efficiency for the two-stage axial and radial-outflow was 13.96% and 12.80% respectively; compared to 10.39%, 10.75% and 9.84% for the single-stage axial, radial-inflow and radial-outflow turbines respectively, with the working fluid R245fa. The results also indicated that the developed small-scale two-stage turbine can be used for a low-temperature (<100 °C) heat source with mass flow rates ranging between 0.1 and 0.5 kg/s for various organic fluids, namely R245fa, R141b and isopentane. These results highlight the potential of using a two-stage turbine configuration to enhance the performance of a small-scale ORC system with low-grade heat sources. Furthermore, these performance maps can provide a good base for selecting a suitable turbine's configuration for the relevant small-scale ORC system driven by low-temperature heat sources. Furthermore, this paper is better than other relevant literature due to considering three types of turbines in single and two stage configuration which showed the effects of turbine performance of each configuration on the ORC thermal efficiency with different operating conditions and working fluids. Eventually, 3D CFD optimization integrated with structural analysis will be developed and applied on these turbines' configurations to improve the peromance of the turbine and ORC system.

Acknowledgement

The main author (Ayad M. Al Jubori) gratefully acknowledges the Iraqi ministry of higher education and scientific research/University of Technology, Baghdad, Iraq for funding the PhD scholarship at the University of Birmingham, UK.

References

Al Jubori, A., Daabo, A., Al-Dadah, R.K., Mahmoud, S. and Ennil, A.B., 2016. Development of micro-scale axial and radial turbines for low-temperature heat source driven organic Rankine cycle. Energy Conversion and Management 130,141-155.

Al Jubori, A., Al-Dadah, R.K., Mahmoud, S., Ennil, A.B. and Rahbar, K., 2017a. Three dimensional optimization of small-scale axial turbine for low temperature heat source driven organic Rankine cycle. Energy Conversion and Management 133, 411-426.

Al Jubori, A.M., Al-Dadah, R.K., Mahmoud, S. and Daabo, A., 2017b. Modelling and parametric analysis of small-scale axial and radial-outflow turbines for Organic Rankine Cycle applications. Applied Energy 190, 981-996.

Balje, O.E., 1981. Turbomachines-A guide to design, selection, and theory. John Wiley & Sons, New York, USA.

Bao, J. and Zhao, L., 2013. A review of working fluid and expander selections for organic Rankine cycle. Renewable and Sustainable Energy Reviews 24, 325-342.

Casati, E., Vitale, S., Pini, M., Persico, G. and Colonna, P., 2014. Centrifugal turbines for mini-organic Rankine cycle power systems. Journal of Engineering for Gas Turbines and Power 136(12), 122607.

Da Lio, L., Manente, G. and Lazzaretto, A., 2014. New efficiency charts for the optimum design of axial flow turbines for organic Rankine cycles. Energy 77, 447-459.

Dixon, S.L. and Hall, C., 2010. Fluid mechanics and thermodynamics of turbomachinery. Butterworth-Heinemann/Elsevier, UK.

Fiaschi, D., Innocenti, G., Manfrida, G. and Maraschiello, F., 2016. Design of micro radial turboexpanders for ORC power cycles: From 0D to 3D. Applied Thermal Engineering 99, 402-410.

Glassman, A.J., 1976. Computer program for design analysis of radial-inflow turbines. NASA TN D-8164, D. C., Washington, USA.

Glassman, A.J., 1992. Computer code for preliminary sizing analysis of axial-flow turbines. NASA NAG3-1165, Lewis Research Center, USA.

Glassman, A.J., 1995. Enhanced analysis and user's manual for radial-inflow turbine conceptual design code RTD. NASA, Contractor Report No. 195454, Lewis Research Center, USA.

Harinck, J., Pasquale, D., Pecnik, R., van Buijtenen, J. and Colonna, P., 2013. Performance improvement of a radial organic Rankine cycle turbine by means of automated computational fluid dynamic design. Proceedings of the Institution of Mechanical Engineers, Part A: J. Power and Energy 227(6), 637-645.

Japikse, D. and Baines, N., 1994. Introduction to turbomachinery. Concepts ETI, USA.

Jones, A.C., 1994. Design and test of a small, high pressure ratio radial turbine. Trans. ASME J. Turbomach. 118(2), 362–370.

Kang, S.H., 2012. Design and experimental study of ORC (organic Rankine cycle) and radial turbine using R245fa working fluid. Energy 41(1), 514-524.

Kang, S.H., 2016. Design and preliminary tests of ORC (organic Rankine cycle) with two-stage radial turbine. Energy 96, 142-154.

Kofskey, M.G. and Nusbaum, W.J., 1968. Aerodynamic evaluation of two-stage axial flow turbine designed for brayton-cycle space power system. NASA TN D-4382, D. C., Washington, USA.

Li, Y. and Ren, X.D., 2016. Investigation of the organic Rankine cycle (ORC) system and the radial-inflow turbine design. Applied Thermal Engineering 96, 547-554.

Moroz, L., Kuo, C.R., Guriev, O., Li, Y.C., and Frolov, B., 2013. Axial turbine flow path design for an organic Rankine cycle using R-245fa. ASME Turbo-Expo 2013: GT2013-94078, V05AT23A004-V05AT23A004.

Moustapha, H., Zelesky, M.F., Baines, N.C. and Japikse, D., 2003. Axial and radial turbines. Concepts NREC, White River Junction, USA.

Pei, G., Li, J., Li, Y., Wang, D. and Ji, J., 2011. Construction and dynamic test of a small-scale organic rankine cycle. Energy 36(5), 3215-3223.

Persico, G., Pini, M., Dossena, V. and Gaetani, P., 2015. Aerodynamics of Centrifugal Turbine Cascades. J. Gas Turbines and Power 137(11), 112602.

Pu, W., Yue, C., Han, D., He, W., Liu, X., Zhang, Q. and Chen, Y., 2016. Experimental study on Organic Rankine cycle for low grade thermal energy recovery. Applied Thermal Engineering 94, 221-227.

Rahbar, K., Mahmoud, S., Al-Dadah, R.K. and Moazami, N., 2016. One-dimensional and three-dimensional numerical optimization and comparison of single-stage supersonic and dual-stage transonic radial inflow turbines for the ORC. Proceedings of the ASME Power and Energy 2016, V001T08A017.

Russell, H., Rowlands, A., Ventura, C. and Jahn, I., 2016. Design and testing process fora 7kw radial inflow refrigerant turbine at the University of Queensland. Proceedings of ASME Turbo Expo, GT2016-58111, V008T23A036.

Sauret, E. and Gu, Y., 2014. Three-dimensional off-design numerical analysis of an organic Rankine cycle radial-inflow turbine. Applied Energy135, 202-211.

Ssebabi, B., Dobson, R.T. and Sebitosi, A.B., 2015. Characterising a turbine for application in an organic Rankine cycle. Energy 93, 1617-1632.

Suhrmann, J.F., Peitsch, D., Gugau, M., Heuer, T. and Tomm, U., 2010. Validation and development of loss models for small size radial turbines. Proceedings of ASME Turbo Expo 2010: power for land, sea and Air GT2010, GT2010-22666, 1937-1949.

Tchanche, B.F., Lambrinos, G., Frangoudakis, A. and Papadakis, G., 2011. Low-grade heat conversion into power using organic Rankine cycles–a review of various applications. Renewable and Sustainable Energy Reviews 15(8), 3963-3979.

Ventura, C.A., Jacobs, P.A., Rowlands, A.S., Petrie-Repar, P. and Sauret, E., 2012. Preliminary design and performance estimation of radial inflow turbines: An automated approach. J. Fluids Eng. 134(3), 031102-13.

Whitfield, A. and Baines, N. C. 1990. Design of radial turbomachines. Longman Scientific & Technical, UK.

Wilson, D.G. and Korakianitis, T., 2014. The design of high-efficiency turbomachinery and gas turbines. MIT press, Massachusetts, USA.

Highlights

- New performance maps for organic Rankine cycle turbines have been presented.
- Axial, radial-inflow and outflow turbines in single and dual stage are considered.
- Design methodology of axial, radial-inflow and outflow turbines is shown.
- High actual ORC thermal efficiency (around 75% of the ideal Carnot Cycle).
- Higher turbine and thermal system efficiencies achieved with two-stage configuration.